



HAL
open science

Carbon-Embedded Tungsten Carbide Electrocatalysts Derived from Self-Deposited Tungsten Oxide for the pH-Universal Hydrogen Evolution Reaction

Chinkit Tyagi, Corinne Lagrost, Vincent Dorcet, Franck Tessier, Bruno Fabre

► **To cite this version:**

Chinkit Tyagi, Corinne Lagrost, Vincent Dorcet, Franck Tessier, Bruno Fabre. Carbon-Embedded Tungsten Carbide Electrocatalysts Derived from Self-Deposited Tungsten Oxide for the pH-Universal Hydrogen Evolution Reaction. ACS Applied Energy Materials, 2023, 6 (12), pp.6842 - 6850. 10.1021/acsaem.3c01236 . hal-04209694

HAL Id: hal-04209694

<https://hal.science/hal-04209694>

Submitted on 19 Sep 2023

HAL is a multi-disciplinary open access archive for the deposit and dissemination of scientific research documents, whether they are published or not. The documents may come from teaching and research institutions in France or abroad, or from public or private research centers.

L'archive ouverte pluridisciplinaire **HAL**, est destinée au dépôt et à la diffusion de documents scientifiques de niveau recherche, publiés ou non, émanant des établissements d'enseignement et de recherche français ou étrangers, des laboratoires publics ou privés.

Carbon-Embedded Tungsten Carbide

Electrocatalysts derived from Self-Deposited

Tungsten Oxide for pH-Universal Hydrogen

Evolution Reaction

Chinkit Tyagi,¹ Corinne Lagrost,¹ Vincent Dorcet,^{1,2} Franck Tessier¹ and Bruno Fabre^{1,}*

¹ CNRS, ISCR (Institut des Sciences Chimiques de Rennes)-UMR6226, Univ Rennes, Rennes F-35000, France

² ScanMAT, Univ Rennes, Rennes F-35000, France

KEYWORDS. Water Splitting, Hydrogen Evolution Reaction, Electrocatalysis, Tungsten Carbides, Nickel foam

ABSTRACT. Tungsten carbide (WC) has been explored as a cost-effective and Earth-abundant alternative electrocatalyst for HER in both acid and alkaline conditions, due to its electronic structure comparable to that of platinum. Herein, we report on a simple and convenient approach for depositing carbon-embedded WC electrocatalyst on nickel foam (NF) from the thermal reduction of a sucrose-impregnated self-deposited tungsten trioxide (WO₃) precursor. Different

sucrose concentrations (between 20 and 80% aqueous solution) and reduction temperatures (between 600 and 1000°C) are tested to achieve an optimized material exhibiting the best electrocatalytic efficiency for HER. The optimized material is obtained from the precursor impregnated with 50% sucrose and thermally reduced at 800°C. It can operate HER with overpotential values measured at 10 and 100 mA cm⁻² of 0.124 and 0.232 V, respectively, at pH 14, and 0.208 and 0.333 V at pH 0.3, respectively. Furthermore, these electrodes are found to be stable in both media during controlled-current density electrolysis tests over a period of 40 h. The presence of excess amorphous carbon embedding WC is beneficial to improve the conductivity and dispersibility of the electrocatalyst, and consequently its HER activity. These findings demonstrate that robust and efficient WC-based binder-free HER electrocatalysts can be produced easily from spontaneously deposited WO₃ film and sucrose as the carbon/carbide source.

1. Introduction

Dihydrogen (H₂) is a clean energy carrier and sustainable alternative to traditional fossil fuels for meeting future energy demands.^{1,2} However, around 95% of global H₂ comes from the steam reforming process,^{3,4} which leads to the emission of greenhouse gases such as carbon dioxide and carbon monoxide.⁵ The development of new routes toward the generation of carbon-free H₂ is a major challenge to be addressed for a successful hydrogen economy.^{6,7} The cleanest method for producing H₂ is through water electrolysis, utilizing renewable energy sources such as wind or solar power.^{8,9,10} Electrochemical water splitting is a promising approach to produce eco-friendly H₂ involving a hydrogen evolution reaction (HER) at the cathode and an oxygen evolution reaction (OER) at the anode.^{11,12} To date, industrially practiced electrocatalysts for water splitting are

mostly based on noble metals such as Pt/Pd for HER and IrO₂/RuO₂ for OER due to their significantly high current density, low onset potential and fast kinetics.¹³ However, the scarcity and high related cost of noble metals have stimulated intensive research in discovering other noble-metal-free and abundant alternatives that can compete with the benchmark electrocatalysts.^{14,15,16} In these recent years, remarkable efforts have been made to develop low-cost transition metal (Ni, Fe, Co, Mo and W) based electrocatalysts for HER including their chalcogenides, phosphides, borides, nitrides, carbides and alloys.^{17,18,19}

In that context, transition metal carbides (TMCs), such as molybdenum and tungsten carbides (Mo_xC and W_xC), are being explored as electrocatalysts for HER. As a matter of fact, combining molybdenum or tungsten with carbon introduces a new d-band which is similar to the Pt d-band. Therefore, due to comparable electronic structures, TMCs are predicted to have Pt-like electrocatalytic activity.^{20,21} In the 1970s, Levy and Boudart provided evidence that tungsten carbide (WC) exhibited Pt-like catalytic activity which was supported by theoretical calculations.²² This behavior is ascribed to the intercalation of carbon atoms into the tungsten lattice, which results in a similar d-band electronic density of states.²³ Since then, WC has been widely investigated as an efficient catalyst for various applications, offering advantages such as low cost, improved electronic conductivity, and high corrosion resistance.²⁴ Hence, WC has been considered as a potential non-noble metal electrocatalyst for HER. Despite its unique properties, pure WC shows low activity for HER in alkaline media.²⁵ Theoretical calculations have demonstrated that the strong adsorption of hydrogen atoms to the WC surface facilitates the reduction of H⁺ but impedes the hydrogen desorption step.²⁶ To address this issue, numerous approaches are being pursued to modify WC by incorporating transition metal (such as Co, Ni and Fe) and heteroatom (such as N, S and P) doping to adjust the electronic properties of the d-band,^{25,26} as well as employing different

conductive catalyst supports to enhance the HER activity.^{27,28} For the latter, carbon and its various forms (e.g., carbon nanotubes and graphene) are widely used as catalyst support to offer a stable, conductive and improved electronic framework by interfacial interactions.^{29,30} For instance, Fan et al., and other research groups reported that the association of WC with different carbon forms was beneficial for various electrocatalytic reactions in strongly alkaline or acidic medium owing to an enhanced charge transfer, minimized corrosion and stabilized WC surface structure.^{27,28,31,32,33} These findings prompted us to develop a cost-effective approach for the elaboration of carbon-supported WC materials showing a pH-universal electrocatalytic activity for HER.

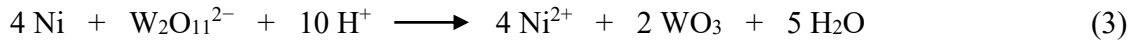
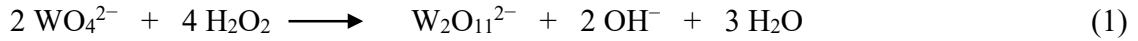
In this work, we report on a facile route to prepare carbon-supported WC on nickel foam (NF) by thermally carbonizing the mixture of a self-deposited tungsten oxide precursor with sucrose as a carbon source. The reductive carburization was performed at different temperatures with various sucrose concentrations in order to obtain an optimized electrocatalyst material operating for HER in alkaline, acidic and neutral conditions. This novel synthesis method constitutes a binder-free approach to design non-precious WC electrocatalysts with high long-term stability for electrochemical H₂ production.

2. Experimental Section

2.1. Chemicals. Nickel foam (NF) with an average pore size of 350 μm was purchased from Recemat B.V. Cell Material Engineering, The Netherlands. Sodium tungstate dihydrate ($\text{Na}_2\text{WO}_4 \cdot 2\text{H}_2\text{O}$), hydrogen peroxide (35% H_2O_2) and KOH were bought from Thermo Fisher Scientific Inc., USA. Sucrose and 20% Pt on graphitized carbon were from Sigma-Aldrich, and nitric acid 68% was purchased from VWR Chemicals, USA. Ultra-pure water (Veolia Water-STI) with a

resistivity of 18.2 MΩ cm was used to prepare the aqueous solutions and all chemicals were used as received without any further purification.

2.2. Self-deposition of WO₃ on nickel foam (NF). Prior to the self-deposition, NF was cleaned with 3M HCl solution, ultrapure water, and absolute ethanol under sonication for 10 min in each solution to remove the oxide layer and was dried at 70°C for 3 h. The deposition solution was obtained by dissolving Na₂WO₄·2H₂O at 0.1 M in ultra-pure water and adding hydrogen peroxide (0.12 M, 35% H₂O₂) dropwise under continuous stirring for 30 min. The pH of the resulting solution was 11.05 ± 0.2. It was adjusted to 0.25 by adding concentrated nitric acid (68% HNO₃) dropwise, then the deposition was performed by dipping cleaned NF (5.0 x 4.5 cm² dimensions) in the solution for 10 min. WO₃-coated NF was rinsed several times with ultra-pure water and finally dried at 90°C. The self-deposition of WO₃ on NF can be explained in the following pathways. The peroxytungstate (W₂O₁₁²⁻) species formed by the reaction of the oxidizing agent (H₂O₂) with WO₄²⁻ (eq. 1) are thermodynamically unstable in highly acidic conditions and slowly decompose to WO₃ following eq. 2.³⁴ Besides this chemical process, WO₃ can also be efficiently electrogenerated from the electrochemical reduction of W₂O₁₁²⁻.^{35,36,37} Herein, it is observed that when NF was immersed into the deposition solution, metallic Ni oxidizes to Ni²⁺ due to the thermodynamically favorable reaction in nitric acid solution.³⁸ As a result, the W₂O₁₁²⁻ ions present in the solution reduce to WO₃ without applying any external potential (eq. 3). In this study, NF not only acts as a substrate but accelerates the deposition process by spontaneous surface redox reactions. It is worth noticing that the self-deposited WO₃ is obtained in the amorphous form. The nature of the metal oxide was revealed by X-ray diffraction after the conversion of the starting amorphous to crystallized material upon heating at 450°C for 4 h in the air (Figure S1 in the Supporting Information).



2.3. Synthesis of WC@C/NF. The self-deposited WO₃-coated NF (**SDW**) sample (1 x 3 cm²) was immersed for 2 min into an aqueous solution containing sucrose at 20, 50 or 80% (w/v) and dried at 90 °C overnight. The resulting material was then thermally reduced at various temperatures with a heating rate of 10 °C/min in a tubular furnace under 5 % H₂/Ar gas flow for 2 h.

2.4. Instrumentation. X-ray diffraction (XRD) patterns of synthesized materials on NF were obtained using a Bruker D8 Advance diffractometer (Cu Kα1 radiation, λ = 1.5406 Å) equipped with a LynxEye fast detector.

Scanning electron microscopy (SEM) images and elemental mapping were performed using a JSM-7100F JEOL microscope and an X-Max 50 mm² EDS detector (Oxford Instruments).

The TEM images and element distribution were probed by scanning transmission electron microscopy (STEM) using a JEOL JEM-2100 LaB₆ instrument operating at 200 kV equipped with an energy-dispersive X-ray spectroscopy (EDS) detector (OXFORD X-MAX^N 80T). The analyzed sample was first prepared by scratching it with a diamond tip. The obtained powder was then crushed manually in ethanol and a drop of the suspension was deposited on a copper grid covered by a carbon film (AGAR S-160 grid).

XPS data have been collected by a NEXSA G2 (ThermoFischer Scientific) spectrometer using the Al Kα X-ray source working at 1486.6 eV and using a spot size of 200 μm². Survey spectra (0-1000 eV) were acquired with an analyzer pass energy of 200 eV (1 eV/step); high-resolution spectra used pass energy of 50 eV (0.1 eV/step). Binding energies were referenced to C 1s peak at 284.8 eV. The core level spectra were peak-fitted using the CasaXPS Software, Ltd. Version

2.3.18. U2 Tougaard or Shirley background subtraction was used for the spectral analysis. The peak areas were normalized by the manufacturer-supplied sensitivity factor ($S_{Cl1s} = 1$, $S_{W4d} = 10.9$, $S_{W4f} = 11.05$, $S_{O1s} = 2.88$, $S_{Ni2p} = 14.18$). For each sample, XPS survey spectra were recorded at three different locations, and we did not observe any difference.

The electrochemical measurements were performed at room temperature on a BioLogic SP-200 single-channel electrochemical workstation equipped with an AC frequency response analyzer (FRA). Modified NF was directly used as the working electrode (geometric surface area: 1 cm^2) and a graphite rod was used as the counter electrode. The reference electrode was either Hg/HgO in an alkaline medium (1.0 M KOH, $\text{pH} = 14 \pm 0.1$) or KCl-saturated Ag/AgCl in acidic (0.5 M H_2SO_4 , $\text{pH} = 0.3$) and neutral (1 M phosphate buffer solution, $\text{pH} = 7.05$) solutions. For comparison, 20 wt% Pt on graphitized carbon, activated carbon and poly(vinylidene fluoride) (PVDF) binder (80:15:5 wt%, respectively) were ground in *N*-methyl-2-pyrrolidone (NMP) to form a slurry, which was then coated onto a freshly cleaned NF piece (1 cm^2 geometric surface area). All HER polarization curves were recorded by linear sweep voltammetry (LSV) at 2 mV s^{-1} with 95% *iR* compensation using the automated *iR*-correction function of the potentiostat. The corresponding Tafel slopes were determined from the linear overpotential vs. \log (current density) (η vs. $\log j$) plots. The current densities were normalized by the geometric surface area of the 3D self-supported NF electrodes and all the measured potentials were converted versus the reversible hydrogen electrode (RHE) according to the equations given below:

In an alkaline medium using a Hg/HgO reference electrode (filled with 1 M KOH solution):

$$E_{\text{RHE}} = E_{\text{Hg/HgO}} + 0.059 \text{ pH} + E^0_{\text{Hg/HgO}} \text{ with } E^0_{\text{Hg/HgO}} = +0.102 \text{ V} \quad (4)$$

In an acidic or neutral medium using an Ag/AgCl reference electrode (filled with saturated KCl solution):

$$E_{\text{RHE}} = E_{\text{Ag/AgCl}} + 0.059 \text{ pH} + E^0_{\text{Ag/AgCl}} \text{ with } E^0_{\text{Ag/AgCl}} = +0.200 \text{ V} \quad (5)$$

where $E_{\text{Hg/HgO}}$ and $E_{\text{Ag/AgCl}}$ are the applied potential values versus the selected reference electrode.

Electrochemical impedance spectroscopy (ESI) measurements were performed at an applied overpotential of 0.2 V over a frequency range from 100 kHz to 100 mHz (50 frequencies, logarithmic distribution) at 10 mV amplitude. To calculate the double-layer capacitance (C_{dl}), cyclic voltammograms (CVs) were recorded in the non-Faradaic region at different scan rates. C_{dl} (in mF cm⁻²) corresponds to the slope of the $\Delta j/2$ vs ν plots where Δj is the difference between the anodic and cathodic charging current densities and ν is the potential scan rate. The long-term stability of the catalytic electrodes was examined using chronopotentiometry at an applied -10 mA cm⁻² current density.

3. Results and Discussion.

3.1. Preparation and Characterization of WC@C/NF. The amorphous self-deposited WO₃-coated NF substrate was first impregnated with sucrose as the carbide source and then heated at different temperatures (600, 800 and 1000°C) under H₂ atmosphere to produce the WC phase. Different sucrose concentrations and temperatures have been tested (Table S1) and their effects on the HER electrocatalytic properties of the resulting materials have been examined. The powder X-ray diffraction (XRD) patterns of materials prepared from self-deposited WO₃ precursor with 50% sucrose and thermally reduced at 600 (**W50C-600**), 800 (**W50C-800**), or 1000 °C (**W50C-1000**) are shown in Figure 1. The diffraction patterns of the precursor heated at 800 and 1000°C confirmed the successful conversion into hexagonal tungsten carbide (WC) phase (JCPDS card no. 00-051-0939) and amorphous carbon along with the presence of cubic nickel (Ni) (JCPDS card no. 00-004-0850) coming from the NF substrate. At a lower temperature of 600°C, the XRD

pattern exhibited characteristic peaks indexed to cubic tungsten (W) (JCPDS card no. 01-089-3728) and Ni with amorphous carbon and a little admixture of monoclinic tungsten oxide (WO₂) phases (JCPDS card no. 01-086-0134).

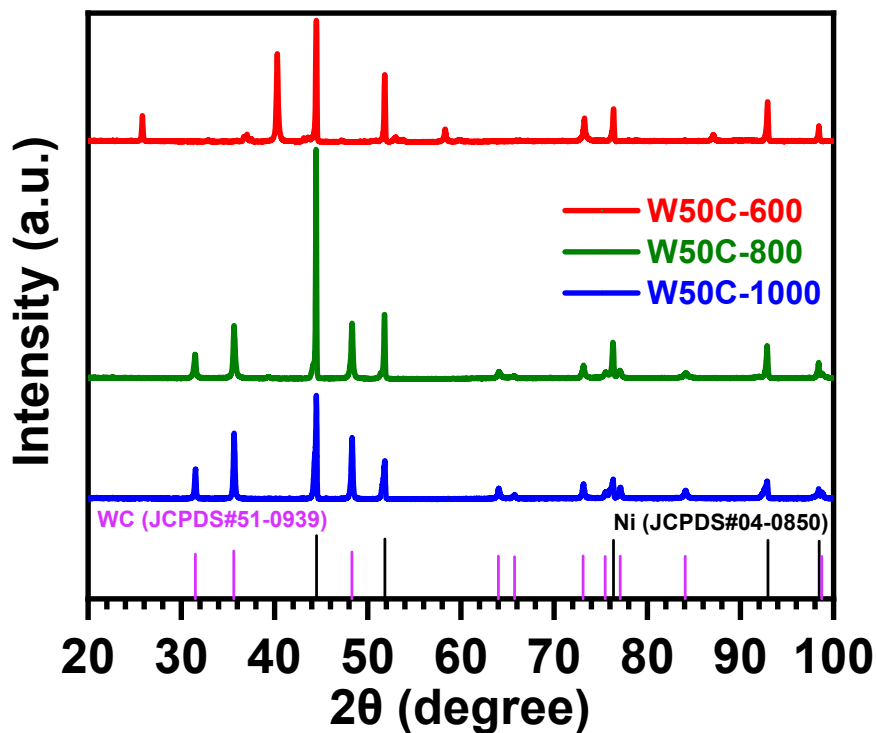


Figure 1. XRD patterns of self-deposited WO₃-coated NF with 50% sucrose solution and thermally reduced at 600°C (**W50C-600**), 800°C (**W50C-800**) or 1000°C (**W50C-1000**) under H₂ atmosphere.

Additionally, the thermal reduction performed with 20 % sucrose solution (**W20C-800**) at an optimized temperature (i.e., 800°C) yielded the formation of cubic W and Ni with tetragonal Ni₄W (JCPDS card no. 03-065-2673) phases and amorphous carbon (Figure S2). Increasing the sucrose concentration to 80% (**W80C-800**) led to a material similar to **W50C-800** with diffraction peaks

characteristic of the hexagonal WC and cubic Ni phases along with excess carbon. We have also checked that the thermal treatment at 800°C of both bare NF with 50% sucrose solution (**NF50C-800**) and self-deposited WO₃-coated NF without sucrose (**W0C-800**) did not lead to the formation of the WC phase. Indeed, the XRD pattern of **NF50C-800** was composed of characteristic peaks of Ni with a little amount of amorphous carbon whereas **W0C-800** was structurally quite similar to **W20C-800** (Figure S3). To sum-up, the optimal WC@C material (**W50C-800**) was obtained from the self-deposited WO₃ precursor impregnated with 50% sucrose solution and thermally reduced at 800°C under H₂ atmosphere. It was therefore selected for further characterization.

The morphological and microstructural characteristics of the optimized material were evaluated by scanning (SEM) and transmission (TEM) electron microscopies. As shown in Figures 2 and S4, the self-deposited WO₃ was characterized by ca. 5 μm-thick porous flake structure uniformly covering Ni foam. The reductive carburization resulted in densification of the network with the appearance of some melted areas. Furthermore, the elemental mapping and energy dispersive X-ray spectroscopy (EDS) analysis of WC@C/NF evidenced the homogeneous distribution of the expected elements, namely W, C and Ni (Figures 2 and S5).

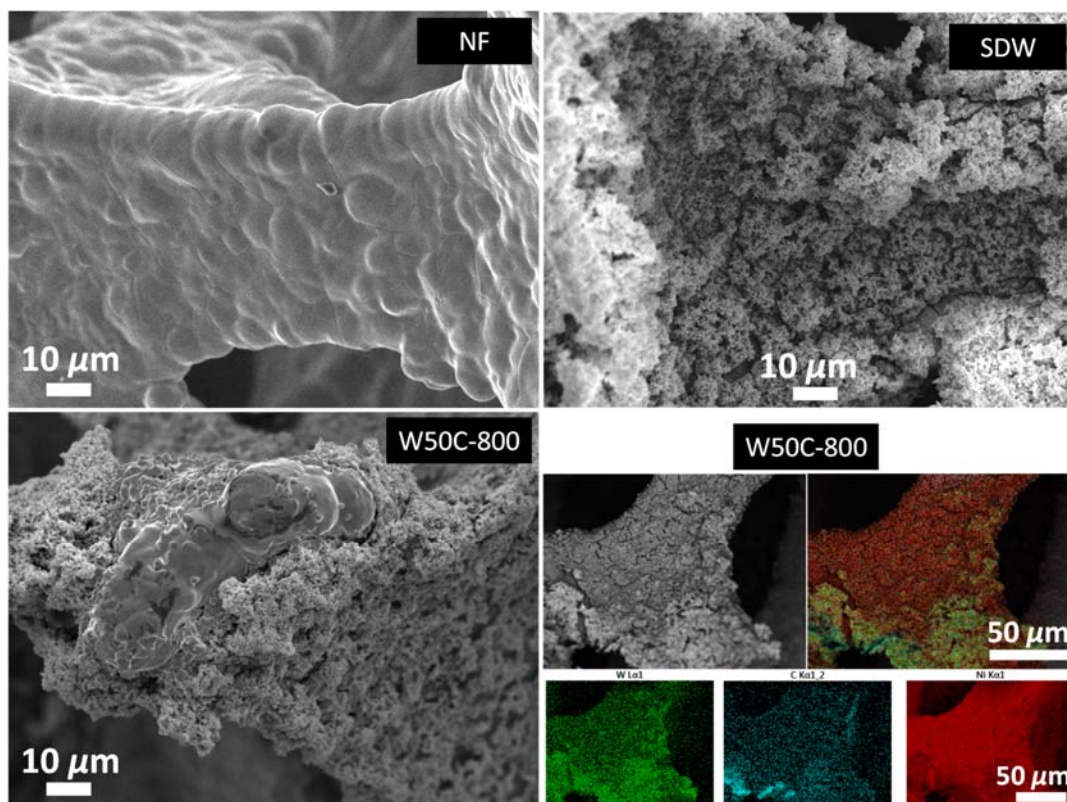


Figure 2. SEM images of bare nickel foam (NF), self-deposited WO_3 -coated NF (SDW) and WC@C/NF (W50C-800). (Bottom right) EDS mapping of WC@C/NF showing the homogeneous distribution of W (green), C (blue) and Ni (red) elements.

The TEM analysis of the WC@C scratched from NF (W50C-800) showed small agglomerates with sizes ranging from 200 nm to 1 μm (dark contrast in Figure 3a). Their elemental analysis confirmed that agglomerated particles consisted of W and C elements with some traces of Ni (Fig. 3d,e and S6). Selected area electron diffraction (SAED) performed on an oriented crystal (inset in Fig. 3a) corresponded to the [010] zone axis of the hexagonal structure of the WC phase (JCPDS card no.: 00-051-0939). This result was corroborated by the high-resolution image showing lattice fringes with a spacing of 2.51 Å which coincides with the (100) planes of the WC phase (Fig. 3b).

As expected, an amorphous carbon phase was also widely present in the sample as displayed in Fig. 3a (light grey colored area at the top right) and the C mapping (Fig. 3e). This phase resulted from the thermal carbonization of sucrose concomitantly with the formation of WC phase.

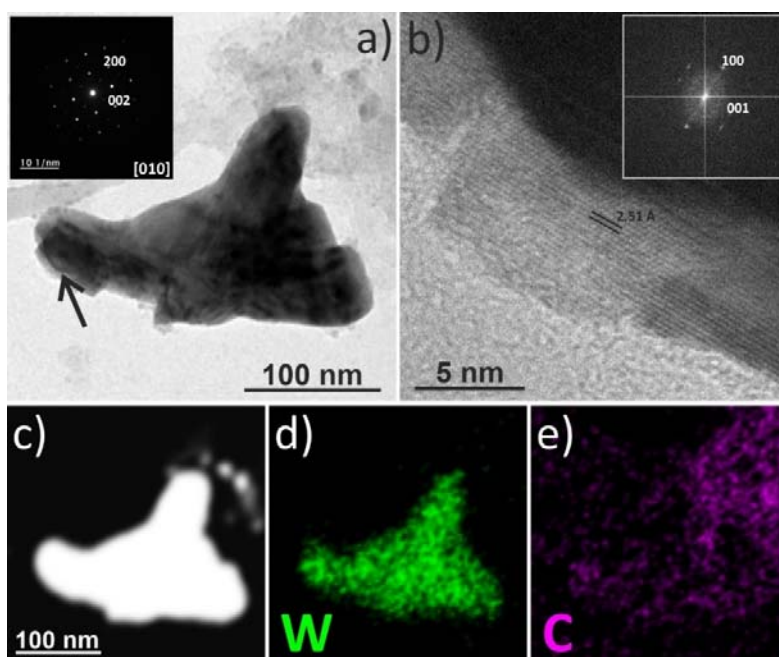


Figure 3. a) Bright field TEM image of an agglomerate from WC@C scratched from NF (**W50C-800**). The inset shows the selected area electron diffraction (SAED) pattern of the crystal pointed by the black arrow. b) High-resolution TEM (HRTEM) image of the area pointed by the arrow in a) with its corresponding fast Fourier transform (FFT) (inset). c) Annular dark field STEM image of the agglomerate and corresponding mapping images of d) W and e) C elements.

The surface composition of the **W50C** samples was probed by X-ray Photoelectron Spectroscopy (XPS) measurements and compared with the **SDW** sample. For all samples, the survey spectra displayed the main peaks corresponding to the elemental species C, O, Ni and W (Figures S7 and S8). The atomic ratios C/Ni, C/W, W/Ni and O/Ni were evaluated from the XPS

survey spectra (Table S2). It can be noticed that the highest values for C/W and C/Ni were obtained for **W50C-800** while the ratio W/Ni was of the same magnitude order for the three **W50C** samples. This observation indicates that **W50C-800** contains more carbon than the two other **W50C** materials while having a content of W closely similar to the whole **W50C** series. High-resolution core level spectra for W 4f and Ni 2p were recorded and peak-fitted to evidence the chemical states of the W and Ni elements. Figure 4 displays the spectra for the **W50C-800** sample. The W 4f spectrum was decomposed into pairs of peaks due to the spin-orbit coupling. The main contribution at 31.8 eV and 34.0 eV was assigned to W^{4+} in WC while the doublet at 36.0 and 38.2 eV was ascribed to WO_3 (W^{6+}).^{39,40,41,42} The presence of a doublet at a higher binding energy than that of the WC contribution (32.5 and 34.7 eV) was attributed to surface-oxidized WC (WC_xO_y).⁴² Interestingly, similar peak-decomposition patterns were observed for **W50C-1000**, however with a slightly higher contribution of the WC component (Table S3), while a strongly different behavior was obtained in the case of **W50C-600** (Figure S9). For this latter, an additional double peak component at 31 and 33.2 eV corresponding to metallic tungsten was also visible and the contribution of WO_3 component with respect to WC components was much larger, indicating an initial formation of WC phase. The **SDW** sample only showed the presence of WO_3 (Fig. S9). The Ni region has also been examined and the Ni 2p_{3/2} signal could be decomposed into three main components (Figures 4 and S9). Metal Ni (852.6 ± 0.2 eV) and Ni^{2+} (856.2 ± 0.2 eV) main lines along with their corresponding satellite peaks and a peak contribution due to interband losses (858.4 ± 0.4 eV) were evidenced.^{43,44,45} A third peak at 853.2 ± 0.4 eV was attributed to the NiW interface (Figures 4 and S9).⁴⁶ In sharp contrast, only the contribution of Ni^{2+} at 856.4 eV could be identified for the **SDW** sample (Fig. S9). These results suggest that an outward diffusion of metallic nickel from the nickel foam occurs to form a NiW interface while the Ni^{2+} contribution is

related to the upmost layer of Ni(OH)₂ of the nickel foam as classically observed for such nickel substrates. The C 1s region spectrum was dominated by the contribution of amorphous carbon and also probably by adventitious carbon, as usually observed in XPS spectra. However, a small contribution at 283.2-283.3 eV was systematically visible for the three **W50C** samples and was consistent with the presence of carbide species (Figure S10).

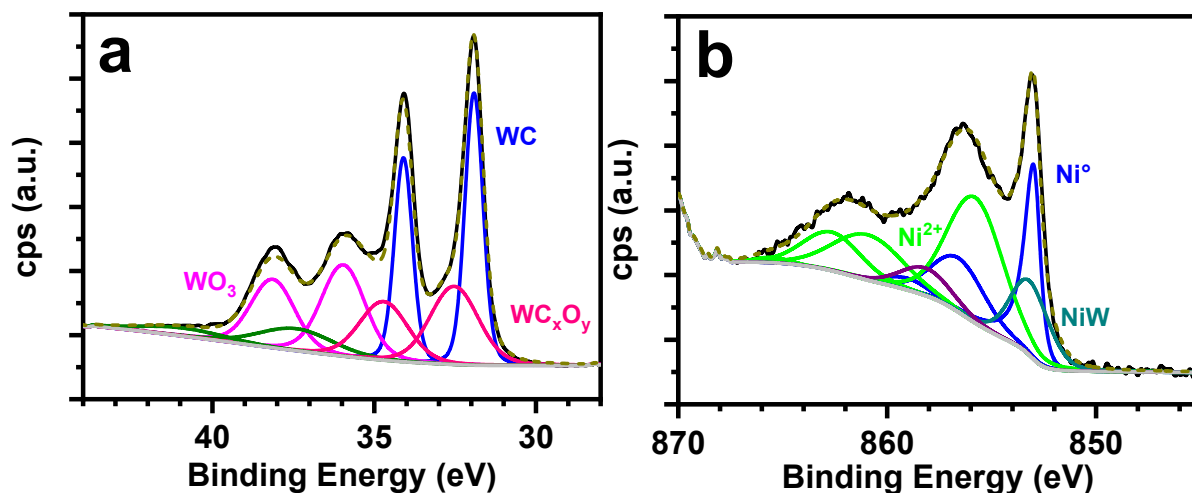


Figure 4. High-resolution core level spectra for the a) W 4f and b) Ni 2p regions with the corresponding fitting decomposition for **W50C-800**. For Ni 2p, only the Ni 2p_{3/2} peak is shown.

3.2. Electrocatalytic Activity for HER. The electrocatalytic activity for HER of the optimized WC@C/NF (**W50C-800**) was first evaluated in alkaline medium (1.0 M KOH, pH 14) and compared with that of other materials prepared in this study (**W50C-600** and **W50C-1000**) along with some reference materials including **NF**, **NF50C-800** and **SDW**. As shown in Figures 5 and S11, **W50C-800** exhibited the highest HER activity, as supported by the lowest *iR*-corrected overpotential values of 0.124 and 0.232 V measured at 10 (η_{10}) and 100 (η_{100}) mA cm⁻², respectively (Table 1). These values are expectedly 106 and 180 mV higher than those determined

for benchmark 20 wt % Pt/C. The lowest activity for HER was obtained for the WC-free materials, for example **W0C-800** and **SDW**, yielding $\eta_{10} = 0.264$ V ($\eta_{100} \sim 0.390$ V) and 0.218 V (0.341 V), respectively. Concerning the two materials containing WC, the superior activity of **W50C-800** with respect to **W50C-1000** could be attributed to the presence of excess amorphous carbon (as supported by XPS analysis, *vide supra*), as previously reported for other thermally carburized W-based materials.^{32,47} This contributes to improve the conductivity and dispersibility of tungsten carbide catalyst, and consequently its HER activity.

The superior activity of **W50C-800** for HER was also confirmed by its Tafel slope of 94 mV dec⁻¹ which was smaller than that of the other prepared electrodes, between 110 and 125 mV dec⁻¹ (Fig. 5b). It is also worth noting that the Tafel slopes calculated for the different materials were between 94 and 125 mV dec⁻¹, which is somewhat higher than that determined for Pt/C electrode (30.7 mV dec⁻¹). These values indicate that the HER process is controlled by the Volmer reaction step, i.e. the adsorption of hydronium ions onto the active sites of the catalysts, whereas the rate-determining step for Pt is the Tafel reaction, i.e. the combination of two adsorbed hydrogen atoms to form molecular H₂.⁴⁸ Although WC has an electronic structure comparable to that of Pt, these differences in the HER kinetics between Pt and our materials could be reasonably explained by the chemical environment of WC (presence of the amorphous carbon and Ni) and the interactions between the different phases.

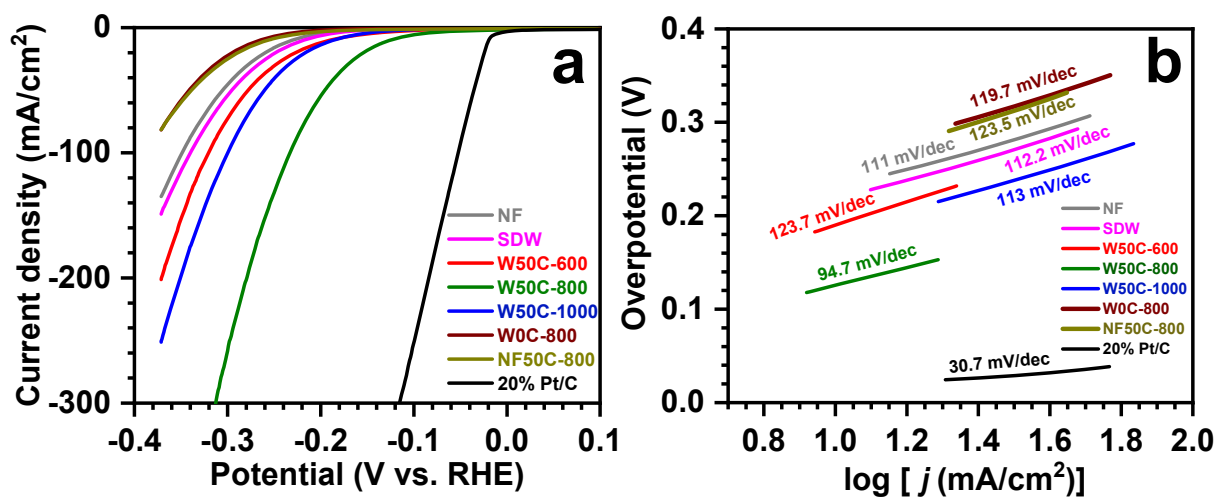


Figure 5. a) *iR*-corrected HER polarization curves at 2 mV/s of bare NF, commercial 20% Pt/C and synthesized materials in 1 M KOH solution and b) corresponding Tafel slopes.

Table 1. HER Electrocatalytic Parameters for Different Modified NF Cathodes in 1 M KOH (pH 14).

Electrode	η_{10} / V^a	η_{100} / V^a	Tafel slope / mV dec^{-1}	R_{ct} / Ω^b
NF	0.229	0.349	111	8.9
SDW	0.218	0.341	112	16.9
W50C-600	0.188	0.319	123	6.5 _s
W50C-800	0.124	0.232	94	2.2
W50C-1000	0.184	0.300	113	5.2
W0C-800	0.264	~0.39	120	26.2
NF50C-800	0.256	~0.39	123	— ^c
20% Pt/C	0.018	0.051	31	0.3

^a Ohmic drop-corrected overpotential for a current density of 10 and 100 mA cm^{-2} . ^b Determined from Nyquist plots at 200 mV overpotential. ^c Not tested.

In order to gain further insights on the electron transfer kinetics, electrochemical impedance spectroscopy (EIS) measurements were performed for all electrodes at an applied overpotential of 0.2 V and in the frequency range 10^5 - 10^{-1} Hz. The data are presented as plots of the imaginary part (Z'') vs the real part (Z') of the complex impedance ($Z = Z' + iZ''$) as a function of frequency f (Nyquist diagram). All Nyquist plots are characterized by a semicircle and can be reasonably fitted by assuming the simplified Randles equivalent electrical circuit comprising a resistance (the cell resistance R_s) in series with the charge transfer resistance (R_{ct}) and a constant phase element (CPE)

in parallel (Figure 6). For this circuit model, the diameter of the semicircle on the Z' axis corresponds to R_{ct} . As expected, the R_{ct} of the electrode **W50C-800** (2.2Ω) was found to be smaller than that calculated for the other electrodes (between 5 and 26 Ω , Table 1) demonstrating faster HER charge transfer kinetics.

In addition, because the electrode substrate is a porous material (namely, NF), it is highly desirable to estimate the electrochemically active surface area (ECSA) for each tested electrode.⁴⁹ A commonly used approach is to determine the electrochemical double-layer capacitance (C_{dl}) from cyclic voltammograms monitored in a non-Faradaic region at different scan rates (Figure S12, see the experimental section for details). C_{dl} is directly proportional to ECSA ($ECSA = C_{dl}/C_s$ where C_s is the specific capacitance of flat Ni)⁵⁰ and is a good indicator of the density of electrocatalytically active sites. In line with other aforementioned electrochemical data, **W50C-800** exhibited the largest C_{dl} value (98.1 mF cm^{-2} , Figure 7) compared with the other electrodes, namely bare **NF** and **SDW** ($\sim 0.3\text{-}0.4 \text{ mF cm}^{-2}$), **W50C-1000** (5.1 mF cm^{-2}) and **W50C-600** (46.2 mF cm^{-2}). This demonstrates that the superior density of active sites in **W50C-800** contributes to the enhanced HER activity. Furthermore, compared with **W50C-1000**, the presence of excess amorphous carbon in **W50C-800** most likely contributes to an increased C_{dl} .

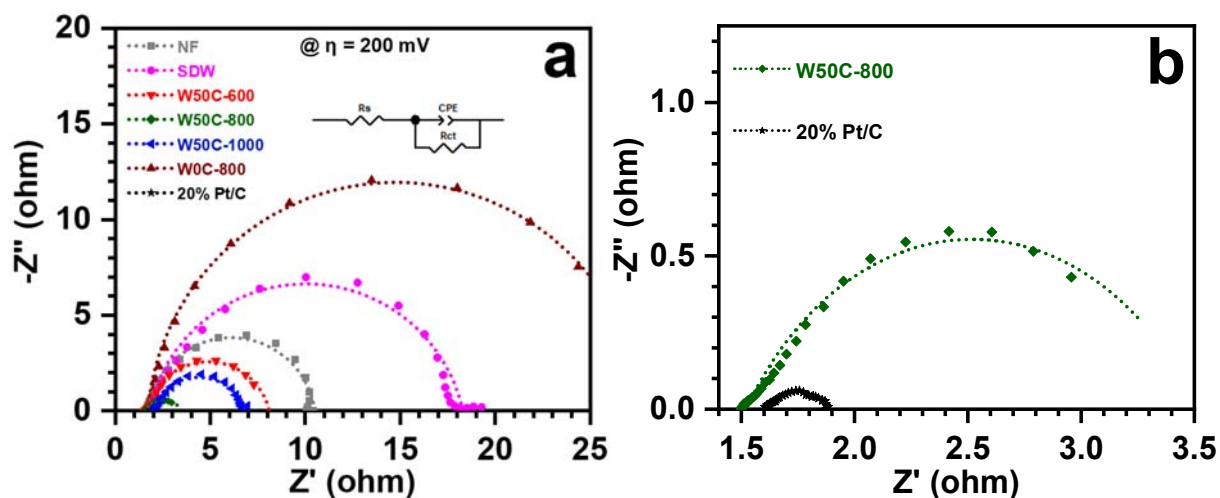


Figure 6. a) EIS Nyquist plots and fitted curves using the selected equivalent electrical circuit (simplified Randles circuit) of bare NF, commercial 20% Pt/C and synthesized materials at an applied overpotential of 0.2 V in 1M KOH. b) Zoomed view of the Nyquist plots obtained for the optimized WC@C/NF material compared with the benchmark 20% Pt/C.

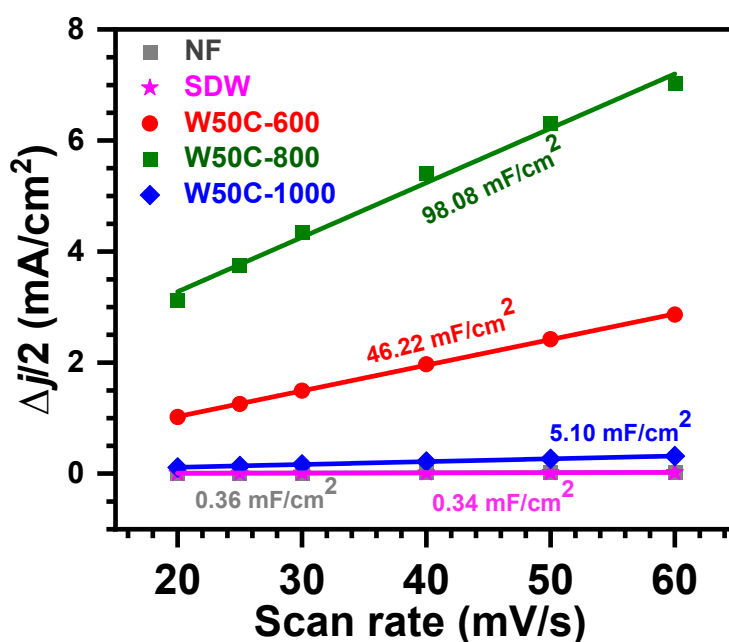


Figure 7. Determination of C_{dl} for the different electrodes from the $\Delta j/2$ vs ν plots where Δj is the difference between the anodic and cathodic charging current densities (taken from cyclic voltammograms shown in Figure S12).

Apart from the electrocatalytic performance, the long-term stability of electrocatalysts carburized at different temperatures (**W50C-600**, **W50C-800** and **W50C-1000**) was also examined at a constant current density of -10 mA cm^{-2} in 1 M KOH solution. The corresponding chronopotentiometric curves showed that **W50C-800** was stabilized at a less negative potential (namely -0.16 V vs RHE) with respect to other electrodes, in relatively good agreement with the potential value derived from the HER polarization curves (Figure 8). Moreover, the two materials containing WC (i.e. **W50C-800** and **W50C-1000**) were found to be the most robust as the potential change was only 60 mV after 40 h electrolysis, while a potential change of 180 mV was monitored for both **W50C-600** and NF electrodes.

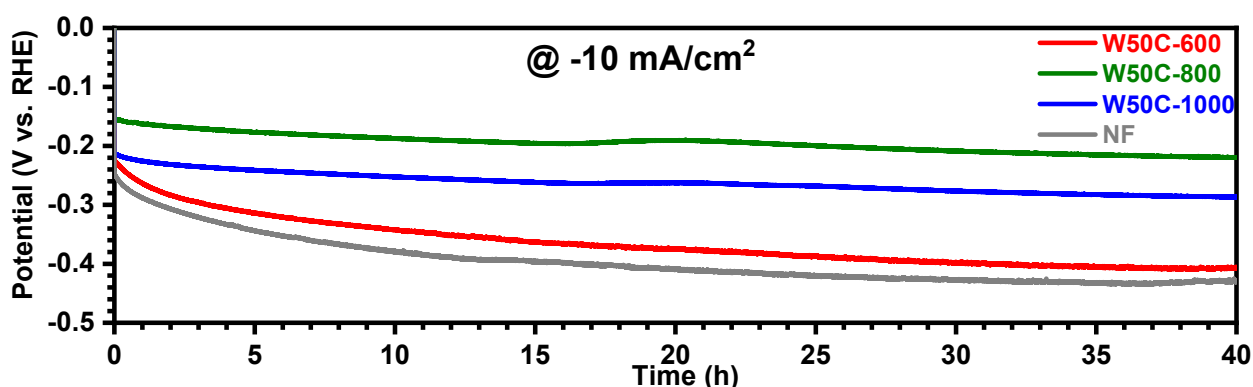


Figure 8. Chronopotentiometric curves of carburized electrocatalysts at an applied current density of -10 mA cm^{-2} in 1M KOH.

After the stability test of **W50C-800** in alkaline medium, XRD data did not show significant changes (Figure S13) while some degradation of the WC deposit was evidenced by XPS. Indeed, the high-resolution core level spectra for the W 4f and Ni 2p regions (Figure S14), as well as the atomic ratios of the characteristic elements (Tables S4 and S5), were consistent with a decrease of the amount of W, a more important contribution of WO_3 and a partial conversion of metal Ni to

Ni²⁺ species (e.g. Ni(OH)₂). Importantly, the active WC phase was still observed which can explain the relatively good catalytic stability of **W50C-800** under operation.

Besides the excellent HER activity in alkaline medium, the HER performance of the optimized WC@C/NF (**W50C-800**) electrode was also evaluated in acidic (0.5 M H₂SO₄, pH = 0.3) and neutral (1 M phosphate buffer solution, pH = 7.0) conditions. It is worth noticing that NF can be used as a electrode for HER for a long time in acidic electrolyte provided that the Ni dissolution is eliminated or strongly limited by applying an overpotential larger than ca. 0.24 V.⁵¹

The η_{10} and η_{100} values measured at pH 0.3 were 0.208 and 0.333 V, respectively, while at pH 7.0, higher overpotentials of 0.298 and 0.577 V were required to achieve 10 and 100 mA cm⁻² current densities, respectively (Figure 9). Compared with bare NF, a ca. 200 mV overpotential gain was observed (Figure S15). Additionally, EIS Nyquist plots recorded at an applied overpotential of 0.2 V yielded R_{ct} values of 8.2 and 29.5 Ω in acidic and neutral conditions, respectively, indicating the electrocatalytic activity for HER of WC@C/NF was weaker at these pHs than at pH 14 (Fig. 9b). Also interestingly, the electrolytic stability of **W50C-800** in acidic conditions was quite comparable to that observed in alkaline solution (Fig. 9c), thus demonstrating its full potential for pH-universal practical H₂ production.

Globally, the electrocatalytic performance for HER of our optimized material in the full pH range compares relatively well with that of other WC-based HER electrocatalysts which were often mixed with an additive polymer matrix, such as Nafion (Table 2). In the case of WC deposited on W, the excellent electrocatalytic HER performance of this material was essentially ascribed to the very small contact resistance due to the formation of chemical bonds between W and WC, allowing electron transport without a barrier. In our study, it is obvious that a significant contact resistance exists between WC and the underlying NF which may impact the HER efficiency.

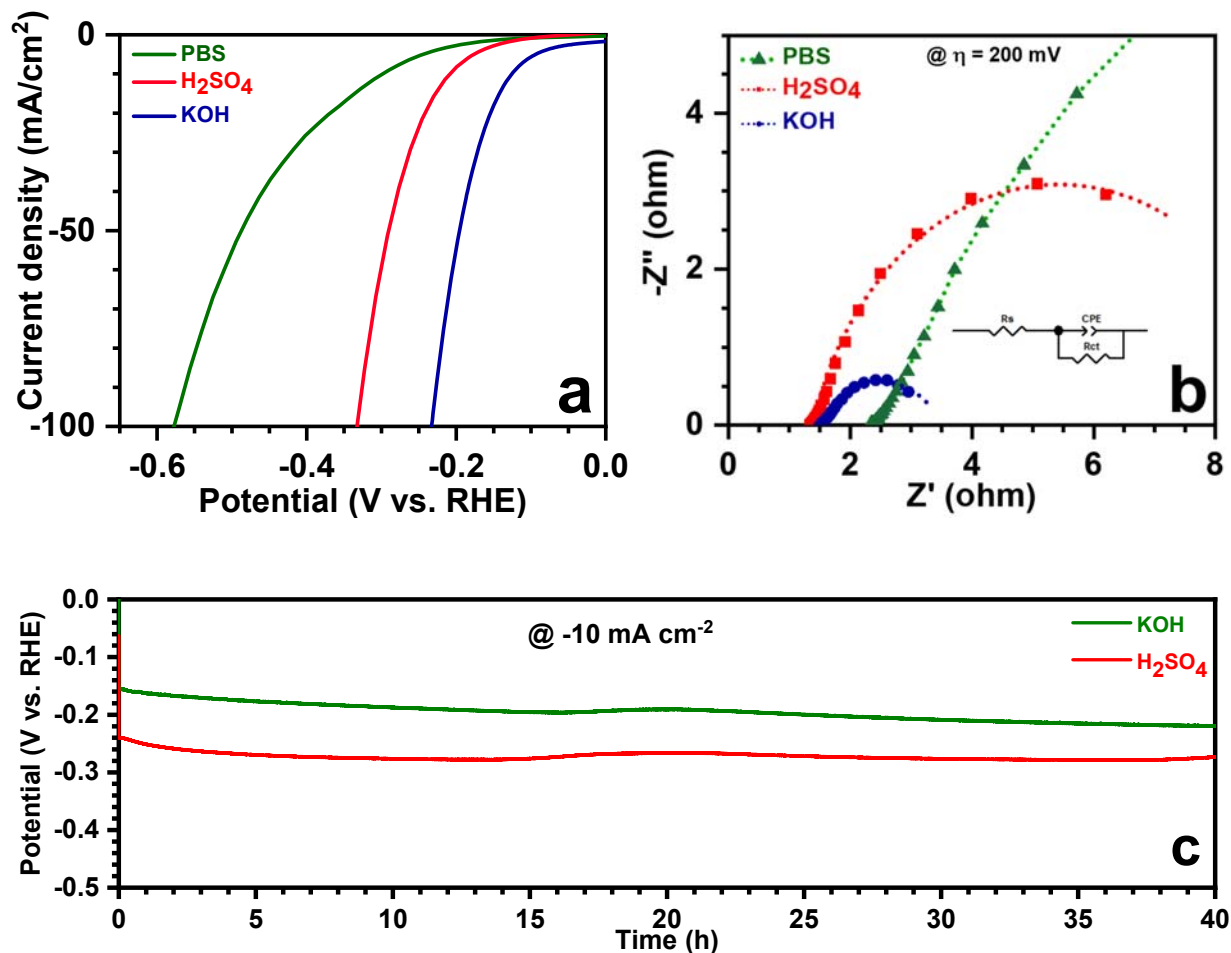


Figure 9. Comparative HER polarization curves at 2 mV/s of WC@C/NF (**W50C-800**) in 1.0 M KOH, 1.0 M PBS, and 0.5 M H₂SO₄ solutions (a) and corresponding EIS Nyquist plots with fitted curves at an applied overpotential of 200 mV (b). (c) Chronopotentiometric curves of **W50C-800** at an applied current density of -10 mA cm⁻² in 1M KOH or 0.5M H₂SO₄.

Table 2. Comparison of the HER activity of WC@C/NF with that of other WC electrocatalysts reported in the literature.

Catalyst	Electrolyte	η_{10} / mV	ref
WC@C on NF ^a	0.5 M H ₂ SO ₄	208	This work
	1 M KOH	124	
	1 M PBS	298	
WC/C composites on glassy carbon ^{a,b}	0.5 M H ₂ SO ₄	220	52
	1 M KOH	208	
	0.1 M PBS	451	
WC/N-doped carbon spheres on GC ^{a,b}	0.5 M H ₂ SO ₄	290	53
	1 M NaOH	300	
WC/graphene on Ga-W substrate ^c	0.5 M H ₂ SO ₄	120	54
	0.1 M KOH	225	
WC/Carbon nanotubes ^c	0.5 M H ₂ SO ₄	145	27
	0.1 M KOH	137	
WC/W₂C@C nanowires ^{a,b} on glassy carbon	0.5 M H ₂ SO ₄	69	55
	1 M KOH	56	
WC on W substrate ^a	0.5 M H ₂ SO ₄	87	56
	1 M KOH	68	
W₂C@WC onto graphite ^a	0.5 M H ₂ SO ₄	310	57
WC and N-doped WC nanoarrays on carbon fiber paper ^d	0.5 M H ₂ SO ₄	193 (WC)	26
		113 (N-doped WC)	
WC/WO_{3-x} porous ceramic membrane ^e	0.5 M H ₂ SO ₄	107	58
	1 M KOH	123	
Ni-doped WC nanocubes on NF ^d	1 M HClO ₄	110	59
	1 M KOH	190	
	0.5 M Na ₂ SO ₄	300	

^a Thermal carburization. ^b Nafion catalyst ink. ^c Chemical vapor deposition growth. ^d Hydrothermal reaction then thermal carburization. ^e Polyethersulfone binder.

4. Conclusion

In this work, WC electrocatalysts embedded with carbon were easily prepared on nickel foam from self-deposited WO_3 precursor followed by reductive carburization using sucrose as the carbon source. The optimized WC@C/NF electrode was produced from the precursor impregnated with a 50% sucrose aqueous solution and then thermally reduced at 800°C under an H_2 atmosphere. WC@C/NF electrocatalyst showed efficient HER activity in both alkaline and acidic media. The overpotential values required to achieve current densities of 10 and 100 mA cm^{-2} were found to be 0.124 and 0.232 V at pH 14, while values of 0.208 and 0.333 V were measured at pH 0.3, respectively. Furthermore, it exhibited reasonably good stability under operation after a 40 h electrolysis in both acidic and alkaline conditions. Globally, the simple and convenient approach proposed herein constitutes a novel, binder-free alternative to pH-universal WC-based HER electrocatalysts and can be extended to other transition-metal carbides. It is also worth mentioning that the HER activity of our materials could be significantly enhanced by incorporating transition metal (such as Co, Ni and Fe) and heteroatom (such as N, S and P) doping to improve the electronic properties of the d-band, as reported for cobalt insertion into WC lattice²⁵ and N-doped WC nanoarrays.²⁶

ASSOCIATED CONTENT

Supporting Information. Additional XRD patterns, SEM images, EDS and XPS spectra, and electrochemical data. The Supporting Information is available free of charge on the ACS Publications website.

AUTHOR INFORMATION

Corresponding Author

* **Bruno Fabre** — CNRS, ISCR (Institut des Sciences Chimiques de Rennes)-UMR6226, Univ Rennes, Rennes F-35000, France. E-mail: bruno.fabre@univ-rennes1.fr

Author Contributions

B. F. and C. T. conceived the project, designed the experiments, analyzed the data and wrote the manuscript. F. T. performed and analyzed the XRD data. C. L. performed and analyzed the XPS data. V. D. performed and analyzed the TEM data. All authors contributed to the results discussion. All authors participated in editing the paper and have given approval to the final version of the manuscript.

Funding Sources

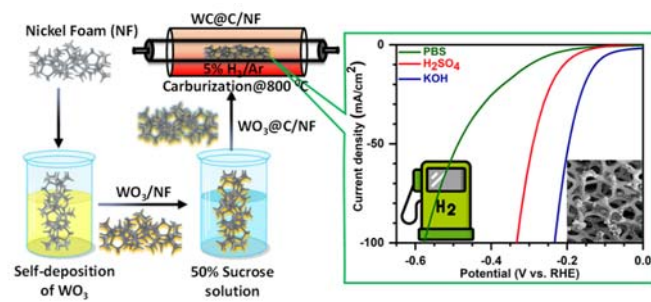
This project has received financial support from the CNRS through the 80|Prime program.

ACKNOWLEDGMENT

Bruno Fabre and Chinkit Tyagi acknowledge the Centre national de la recherche scientifique (CNRS) for the research funding and PhD. research grant (80|Prime program). The XRD, TEM and XPS measurements have been performed on OSIRIX, THEMIS and ASPHERYX platforms, respectively (ScanMAT, UAR 2025 University of Rennes-CNRS; CPER-FEDER 2015-2020). The authors are grateful to Stéphanie Lamy for her assistance in XRD experiments and to James

Behan for fruitful discussion. Loic Joanny and Francis Gouttefangeas are fully acknowledged for SEM images and EDS analyses performed at CMEBA (ScanMAT, University of Rennes).

Table of Contents (TOC)



REFERENCES

- (1) Lewis, N. S.; Nocera, D. G. Powering the Planet: Chemical Challenges in Solar Energy Utilization. *Proc. Natl. Acad. Sci. U. S. A.* **2006**, *103*, 15729-15735.
- (2) International Energy Agency, *The Future of Hydrogen*, International Energy Agency technical report, 2019.
- (3) United States Department of Energy. *A National Vision of America's Transition to a Hydrogen Economy—To 2030 and Beyond*; Washington, DC, 2003.
- (4) European Commission, *A Hydrogen Strategy for a Climate Neutral Europe* [COM(2020) 301 final], European Commission technical report, 2020.
- (5) Acar, C.; Dincer, I. The Potential Role of Hydrogen as a Sustainable Transportation Fuel to Combat Global Warming. *Int. J. Hydrogen Energy* **2020**, *45*, 3396–3406.
- (6) Turner, J. A. Sustainable Hydrogen Production. *Science* **2004**, *305*, 972–974.
- (7) Seh, Z. W.; Kibsgaard, J.; Dickens, C. F.; Chorkendorff, I.; Nørskov, J. K.; Jaramillo, T. F. Combining Theory and Experiment in Electrocatalysis: Insights into Materials Design. *Science* **2017**, *355*, eaad4998.
- (8) McHugh, P. J.; Stergiou, A. D.; Symes, M. D. Decoupled Electrochemical Water Splitting: From Fundamentals to Applications, *Adv. Energy Mater.* **2020**, *10*, 2002453.
- (9) Lagadec, M. F.; Grimaud, A. Water Electrolysers with Closed and Open Electrochemical Systems. *Nat. Mater.* **2020**, *19*, 1140–1150.
- (10) Terlouw, T.; Bauer, C.; McKenna, R.; Mazzotti, M. Large-Scale Hydrogen Production via Water Electrolysis: a Techno-Economic and Environmental Assessment. *Energy Environ. Sci.* **2022**, *15*, 3583-3602.

-
- (11) You, B.; Sun, Y. Innovative Strategies for Electrocatalytic Water Splitting, *Acc. Chem. Res.* **2018**, *51*, 1571–1580.
- (12) Yu, Z.-Y.; Duan, Y.; Feng, X.-Y.; Yu, X.; Gao, M.-R.; Yu, S.-H. Clean and Affordable Hydrogen Fuel from Alkaline Water Splitting: Past, Recent Progress, and Future Prospects. *Adv. Mater.* **2021**, *33*, 2007100.
- (13) Wei, C.; Rao, R. R.; Peng, J.; Huang, B.; Stephens, I. E. L.; Risch, M.; Xu, Z. J.; Shao-Horn, Y. Recommended Practices and Benchmark Activity for Hydrogen and Oxygen Electrocatalysis in Water Splitting and Fuel Cells. *Adv. Mater.* **2019**, *31*, 1806296.
- (14) Roger, I.; Shipman, M. A.; Symes, M. D. Earth-Abundant Catalysts for Electrochemical and Photoelectrochemical Water Splitting. *Nat. Rev. Chem.* **2017**, *1*, 0003.
- (15) McCrory, C. C. L.; Jung, S.; Ferrer, I. M.; Chatman, S. M.; Peters, J. C.; Jaramillo, T. F. Benchmarking Hydrogen Evolving Reaction and Oxygen Evolving Reaction Electrocatalysts for Solar Water Splitting Devices. *J. Am. Chem. Soc.* **2015**, *137* (13), 4347–4357.
- (16) Li, A.; Sun, Y.; Yao, T.; Han, H. Earth-Abundant Transition-Metal-Based Electrocatalysts for Water Electrolysis to Produce Renewable Hydrogen. *Chem. Eur. J.* **2018**, *24*, 18334-18355.
- (17) Anantharaj, S.; Ede, S. R.; Sakthikumar, K.; Karthick, K.; Mishra, S.; Kundu, S. Recent Trends and Perspectives in Electrochemical Water Splitting with an Emphasis on Sulfide, Selenide, and Phosphide Catalysts of Fe, Co, and Ni: A Review. *ACS Catal.* **2016**, *6*, 8069–8097.
- (18) Zhong, Y.; Xia, X. H.; Shi, F.; Zhan, J. Y.; Tu, J. P.; Fan, H. J. Transition Metal Carbides and Nitrides in Energy Storage and Conversion. *Adv. Sci.* **2016**, *3*, 1500286.
- (19) Benck, J. D.; Hellstern, T. R.; Kibsgaard, J.; Chakhranont, P.; Jaramillo, T. F. Catalyzing the Hydrogen Evolution Reaction (HER) with Molybdenum Sulfide Nanomaterials. *ACS Catal.* **2014**, *4*, 3957–3971.

-
- (20) Zou, X.; Zhang, Y. Noble Metal-Free Hydrogen Evolution Catalysts for Water Splitting. *Chem. Soc. Rev.* **2015**, *44*, 5148–5180.
- (21) Liu, Y.; Kelly, T. G.; Chen, J. G.; Mustain, W. E. Metal Carbides as Alternative Electrocatalyst Supports. *ACS Catal.* **2013**, *3*, 1184–1194.
- (22) Levy, R. B.; Boudart, M. Platinum-like Behavior of Tungsten Carbide in Surface Catalysis. *Science* **1973**, *181*, 547–549.
- (23) Bennett, L. H.; Cuthill, J. R.; Mcalister, A. J.; Erickson, N. E.; Watson, R. E. Electronic Structure and Catalytic Behavior of Tungsten Carbide. *Science* **1974**, *184*, 563–565.
- (24) Ren, B.; Li, D.; Jin, Q.; Cui, H.; Wang, C. Novel Porous Tungsten Carbide Hybrid Nanowires on Carbon Cloth for High-Performance Hydrogen Evolution. *J. Mater. Chem. A* **2017**, *5*, 13196–13203.
- (25) Jin, H.; Chen, J.; Mao, S.; Wang, Y. Transition Metal Induced the Contraction of Tungsten Carbide Lattice as Superior Hydrogen Evolution Reaction Catalyst. *ACS Appl. Mater. Interfaces* **2018**, *10*, 22094–22101.
- (26) Han, N.; Yang, K. R.; Lu, Z.; Li, Y.; Xu, W.; Gao, T.; Cai, Z.; Zhang, Y.; Batista, V. S.; Liu, W.; Sun, X. Nitrogen-Doped Tungsten Carbide Nanoarray as an Efficient Bifunctional Electrocatalyst for Water Splitting in Acid. *Nat. Commun.* **2018**, *9*, 924.
- (27) Fan, X.; Zhou, H.; Guo, X. WC Nanocrystals Grown on Vertically Aligned Carbon Nanotubes: An Efficient and Stable Electrocatalyst for Hydrogen Evolution Reaction. *ACS Nano* **2015**, *9*, 5125–5134.
- (28) Yan, P.; Wu, Y.; Wei, X.; Zhu, X.; Su, W. Preparation of Robust Hydrogen Evolution Reaction Electrocatalyst WC/C by Molten Salt. *Nanomaterials* **2020**, *10*, 1–11.

-
- (29) Liu, Y.; Wang, Q.; Zhang, J.; Ding, J.; Cheng, Y.; Wang, T.; Li, J.; Hu, F.; Yang, H. Bin; Liu, B. Recent Advances in Carbon-Supported Noble-Metal Electrocatalysts for Hydrogen Evolution Reaction: Syntheses, Structures, and Properties. *Adv. Energy Mater.* **2022**, *12*, 2200928.
- (30) Wang, J.; Kim, J.; Choi, S.; Wang, H.; Lim, J. A Review of Carbon-Supported Nonprecious Metals as Energy-Related Electrocatalysts. *Small Methods.* **2020**, *4*, 2000621.
- (31) Bosco, J. P.; Sasaki, K.; Sadakane, M.; Ueda, W.; Chen, J. G. Synthesis and Characterization of Three-Dimensionally Ordered Macroporous (3DOM) Tungsten Carbide: Application to Direct Methanol Fuel Cells. *Chem. Mater.* **2010**, *22*, 966–973.
- (32) Liu, Z.; Li, P.; Zhai, F.; Wan, Q.; Volinsky, A. A.; Qu, X. Amorphous Carbon Modified Nano-Sized Tungsten Carbide as a Gas Diffusion Electrode Catalyst for the Oxygen Reduction Reaction. *RSC Adv.* **2015**, *5*, 70743–70748.
- (33) Chen, W. F.; Schneider, J. M.; Sasaki, K.; Wang, C. H.; Schneider, J.; Iyer, S.; Iyer, S.; Zhu, Y.; Muckerman, J. T.; Fujita, E. Tungsten Carbide–Nitride on Graphene Nanoplatelets as a Durable Hydrogen Evolution Electrocatalyst. *ChemSusChem* **2014**, *7*, 2414–2418.
- (34) Meulenkamp, E. A. Mechanism of WO₃ Electrodeposition from Peroxy-Tungstate Solution. *J. Electrochem. Soc.* **1997**, *144*, 1664–1671.
- (35) Yun, G.; Balamurugan, M.; Kim, H. S.; Ahn, K. S.; Kang, S. H. Role of WO₃ Layers Electrodeposited on SnO₂ Inverse Opal Skeletons in Photoelectrochemical Water Splitting. *J. Phys. Chem. C* **2016**, *120*, 5906–5915.
- (36) Reyes-Gil, K. R.; Stephens, Z. D.; Stavila, V.; Robinson, D. B. Composite WO₃/TiO₂ Nanostructures for High Electrochromic Activity. *ACS Appl. Mater. Interfaces* **2015**, *7*, 2202–2213.
- (37) Kondrachova, L.; Hahn, B. P.; Vijayaraghavan, G.; Williams, R. D.; Stevenson, K. J. Cathodic

Electrodeposition of Mixed Molybdenum Tungsten Oxides from Peroxo-Polymolybdotungstate Solutions. *Langmuir* **2006**, *22*, 10490–10498.

(38) R Dhar, B. N. Action of Nitric Acid on Metals. *J. Phys. Chem.* **2002**, *29*, 142–159.

(39) Colton, R. J.; Rabalais, J. W. Electronic Structure of Tungsten and Some of its Borides, Carbides, Nitrides, and Oxides by X-ray Electron Spectroscopy. *Inorg. Chem.* **1976**, *15*, 236-238.

(40) Sivkov, D.; Nekipelov, S.; Petrova, O.; Vinogradov, A.; Mingaleva, A.; Isaenko, S.; Makarov, P.; Ob'edkov, A.; Kaverin, B.; Gusev, S.; Vilkov, I.; Aborkin, A.; Sivkov, V. Studies of Buried Layers and Interfaces of Tungsten Carbide Coatings on the MWCNT Surface by XPS and NEXAFS Spectroscopy. *Appl. Sci.* **2020**, *10*, 4736-4757.

(41) Zellner, M. B.; Chen, J. G. Surface Science and Electrochemical Studies of WC and W₂C PVD Films as Potential Electrocatalysts. *Catal. Today* **2005**, *99*, 209-307.

(42) Krasovskii, P. V.; Malinovskaya, O. S.; Samokhin, A. V.; Blagoveshchenskiy, Y. V.; Kazakov, V. A.; Ashmarin, A. A. XPS Study of Surface Chemistry of Tungsten Carbides Nanopowders Produced through DC Thermal Plasma/Hydrogen Annealing Process. *Appl. Surf. Sci.* **2015**, *339*, 46-54.

(43) Grosvenor, A. P.; Biesinger, M. C.; Smart, R. St. C.; McIntyre, N. S. New Interpretations of XPS Spectra of Nickel Metal and Oxides. *Surf. Sci.* **2006**, *600*, 1771–1779.

(44) Biesinger, M. C.; Payne, B. P.; Lau, L. W. M; Gerson, A.; Smart, R. St. C. X-Ray Photoelectron Spectroscopic Chemical State Quantification of Mixed Nickel Metal Oxide and Hydroxide Systems. *Surf. Interface Anal.* **2009**, *41*, 324-332.

(45) Biesinger, M. C.; Payne, B. P.; Grosvenor, A.; Lau, L. W. M.; Gerson, A.; Smart, R. St. C. Resolving Surface Chemical States in XPS Analysis of First Row Transition Metals Oxides and Hydroxides: Cr, M, Fe, Co and Ni. *Appl. Surf. Sci.* **2011**, *257*, 2717-2730.

-
- (46) Xiong, B.; Zhao, W.; Tian, H.; Huang, W.; Chen, L.; Shi, J. Nickel-Tungsten Nano-Alloying for High Performance Hydrogen Electro-Catalytic Oxidation. *Chem. Eng. J.* **2022**, *432*, 134189.
- (47) Tomas-Garcia, A. L.; Li, Q.; Jensen, J. O.; Bjerrum, N. J. High Surface Area Tungsten Carbides: Synthesis, Characterization and Catalytic Activity towards the Hydrogen Evolution Reaction in Phosphoric Acid at Elevated Temperatures. *Int. J. Electrochem. Sci.* **2014**, *9*, 1016-1032.
- (48) Murthy, A. P.; Theerthagiri, J.; Madhavan, J. Insights on Tafel Constant in the Analysis of Hydrogen Evolution Reaction. *J. Phys. Chem. C* **2018**, *122*, 23943-23949.
- (49) Trasatti, S.; Petrii, O.A. Real Surface Area Measurements in Electrochemistry. *Pure Appl. Chem.* **1991**, *63*, 711-734.
- (50) McCrory, C. C. L.; Jung, S.; Peters, J. C.; Jaramillo, T. F. Benchmarking Heterogeneous Electrocatalysts for the Oxygen Evolution Reaction. *J. Am. Chem. Soc.* **2013**, *135*, 16977–16987.
- (51) Lu, J.; Xiong, T.; Zhou, W.; Yang, L.; Tang, Z.; Chen, S. Metal Nickel Foam as an Efficient and Stable Electrode for Hydrogen Evolution Reaction in Acidic Electrolyte under Reasonable Overpotentials. *ACS Appl. Mater. Interfaces* **2016**, *8*, 5065-5069.
- (52) Liu, C.; Zhou, J.; Xiao, Y.; Yang, L.; Yang, D.; Zhou, D. Structural and Electrochemical Studies of Tungsten Carbide/Carbon Composites for Hydrogen Evolution. *Int. J. Hydrogen Energy* **2017**, *42*, 29781–29790.
- (53) Han, L.; Xu, M.; Han, Y.; Yu, Y.; Dong, S. Core-Shell-Structured Tungsten Carbide Encapsulated within Nitrogen-Doped Carbon Spheres for Enhanced Hydrogen Evolution. *ChemSusChem* **2016**, *9*, 2784–2787.

-
- (54) Zeng, M.; Chen, Y.; Li, J.; Xue, H.; Mendes, R. G.; Liu, J.; Zhang, T.; Rummeli, M. H.; Fu, L. 2D WC Single Crystal Embedded in Graphene for Enhancing Hydrogen Evolution Reaction. *Nano Energy* **2017**, *33*, 356–362.
- (55) Zhang, L. N.; Ma, Y. Y.; Lang, Z. L.; Wang, Y. H.; Khan, S. U.; Yan, G.; Tan, H. Q.; Zang, H. Y.; Li, Y. G. Ultrafine Cable-like WC/W₂C Heterojunction Nanowires Covered by Graphitic Carbon towards Highly Efficient Electrocatalytic Hydrogen Evolution. *J. Mater. Chem. A* **2018**, *6*, 15395–15403.
- (56) Huang, J.; Hong, W.; Li, J.; Wang, B.; Liu, W. High-Performance Tungsten Carbide Electrocatalysts for the Hydrogen Evolution Reaction. *Sustain. Energy Fuels* **2020**, *4*, 1078–1083.
- (57) Emin, S.; Altinkaya, C.; Semerci, A.; Okuyucu, H.; Yildiz, A.; Stefanov, P. Tungsten Carbide Electrocatalysts Prepared from Metallic Tungsten Nanoparticles for Efficient Hydrogen Evolution. *Appl. Catal. B Environ.* **2018**, *236*, 147–153.
- (58) Wang, F.; Dong, B.; Wang, J.; Ke, N.; Tan, C.; Huang, A.; Wu, Y.; Hao, L.; Yin, L.; Xu, X.; Xian, Y.; Agathopoulos, S. Self-Supported Porous Heterostructure WC/WO_{3-x} Ceramic Electrode for Hydrogen Evolution Reaction in Acidic and Alkaline Media. *J. Adv. Ceram.* **2022**, *11*, 1208–1221.
- (59) Chen, Y.; Zheng, Y.; Yue, X.; Huang, S. Hydrogen Evolution Reaction in Full pH Range on Nickel Doped Tungsten Carbide Nanocubes as Efficient and Durable Non-Precious Metal Electrocatalysts. *Int. J. Hydrogen Energy* **2020**, *45*, 8695–8702.